

## Ice nucleation characteristics of an isolated wave cloud

By R. J. COTTON<sup>1\*</sup> and P. R. FIELD<sup>1</sup>

<sup>1</sup>*Meteorological Office, UK*

(Received 1 January 2001; revised 31 December 2001)

### SUMMARY

This paper reports on a series of simulations of a single isolated gravity wave cloud measured during the INTACC (INteraction of Aerosol and Cold Clouds) campaign. Using a parcel model with explicit liquid and ice phase microphysics, a number of different heterogeneous nucleation modes have been tested. It has been impossible for the model to reproduce, using any of the usual nucleation modes, both the observed peak ice number concentration and ice water content while not affecting the liquid water part of the cloud. The key to simulating both of these simultaneously appears to lie in most ice nucleation occurring very rapidly at a critical time during evaporation of the liquid droplets in the downdraught of the lee wave.

KEYWORDS: Ice nucleation Wave cloud Parcel model

### 1. INTRODUCTION

The radiative properties of ice clouds depends on their microphysical properties, such as ice water content, size spectra and crystal habit. The primary ice nucleation determines the ice production rate and size spectra, so an understanding of ice nucleation is necessary if ice clouds are to be modelled correctly. The study of ice nucleation in cirrus is hampered by the difficulty in measuring the environmental conditions and an uncertainty in the age of the ice crystals sampled. Orographic lenticular wave clouds however provide a simpler dynamical and microphysical environment.

In cold clouds, with temperatures below  $-35^{\circ}\text{C}$ , the dominant ice nucleation mode is homogeneous freezing of the supercooled water droplets with the nucleation rate increasing very rapidly for colder temperatures. Nucleation rates obtained from laboratory measurements, field studies, and theoretical work all agree well (Sassen and Dodd 1988; Heymsfield and Miloshevich 1993; Pruppacher 1995). For example, Heymsfield and Miloshevich used a numerical model to show that the observed properties of a cold lenticular cloud were consistent with homogeneous freezing of solution droplets.

At temperatures warmer than  $-30^{\circ}\text{C}$ , homogeneous freezing is negligible and ice nucleation must take place heterogeneously. Heterogeneous ice nucleation uses ice forming nuclei (IN) which are a special subset of atmospheric aerosols. Several heterogeneous nucleation modes are recognised:

- Deposition nucleation where water vapour is absorbed directly onto the surface of the IN where it is transformed into ice.
- Condensation-freezing where, above water saturation, a film of liquid is first formed on the surface of the IN and then the condensate freezes.
- Contact-freezing where the IN initiates freezing at the moment of its contact with a supercooled water drop.
- Immersion freezing nucleation where freezing of droplets is induced by IN located within the droplets themselves.

A more uncertain ice nucleation mode involves the aerosol particles resulting from evaporation of cloud droplets (Khain *et al.* 2000). During evaporation of charged droplets the

\* Corresponding author: Cloud Physics Research, Met Office, Building Y46, DERA, Farnborough, Hampshire, GU14 0LX, UK. e-mail: richard.cotton@metoffice.com

charge is accumulated on the surface of the aerosol and these 'evaporation nuclei' are thought to be effective ice-forming nuclei (Beard 1992; Rosinski and Morgan 1991). If the environment also contains incompletely evaporated supercooled droplets, electroscavenging of the charged evaporation nuclei can significantly enhance the contact-freezing rate (Tinsley *et al.* 2000).

Despite many field studies and laboratory experiments, there are still uncertainties in IN concentrations and in the nucleation modes that occur in clouds. Cold wave clouds were sampled during the Subsonic Aircraft: Contrail and Cloud Effects Special Study (SUCCESS). Modelling by Jensen *et al.* (1998) of two wave cloud cases (at  $-37^{\circ}\text{C}$  and  $-62^{\circ}\text{C}$ ) show that deposition IN concentrations were less than  $0.5\text{ cm}^{-3}$ . Rogers *et al.* (1998) show that deposition or condensation-freezing IN concentrations measured during SUCCESS using a continuous flow chamber were between  $0.001$  and  $0.1\text{ cm}^{-3}$ . Cooper and Vali (1981) observed mountain cap clouds over  $-15^{\circ}\text{C}$  to  $-20^{\circ}\text{C}$  and concluded that most ice formed during the initial liquid condensation process and that condensation-freezing or contact nucleation were the probable nucleation modes. Demott (1990) performed laboratory studies on soot particles using a continuous slow expansion cloud chamber and suggested that immersion freezing is a dominant mode for ice production at temperatures warmer than  $-34^{\circ}\text{C}$ .

In this paper we will report on a model-observation comparison of a single stationary isolated gravity wave cloud. This cloud had significant liquid water and ice at all heights with the temperature varying from  $-18^{\circ}\text{C}$  at cloud base to  $-32^{\circ}\text{C}$  at cloud top. Heterogeneous nucleation was therefore expected to be dominant. A detailed microphysical and dynamical model was used to accurately simulate the observed wave cloud with the primary aim of determining the characteristics of the ice nucleation and determine which, if any, of the above mentioned heterogeneous nucleation schemes were dominant. The new aircraft instruments used in this study will be briefly described, and the observations from some aircraft runs through the cloud will then be shown. The model used to simulate the cloud will then be described in some detail, followed by the model-observation comparisons.

## 2. INSTRUMENTATION

The Met Office C-130 aircraft carried standard instrumentation which included: wind vanes, inertial navigation unit and GPS to measure vertical and horizontal winds, Rosemount probes (de-iced platinum resistance thermometer), a General Eastern cooled mirror device to measure frost point, a Lyman- $\alpha$  evaporator hygrometer to measure total water content (TWC), a Johnson-Williams liquid water hot wire probe, a PMS (Particle Measuring Systems) 2D-C probe to measure cloud particle concentration, and a PMS PCASP (passive cavity aerosol spectrometer probe) and a CN (condensation nucleus) counter to measure aerosol concentrations. See Rogers *et al.* (1995) for further discussion, and Quante *et al.* (1996) for information on the accuracy of the wind and temperature measurements.

Various new instruments were also carried (see Field 2001 for more details):

- A laser scattering device, SID (small ice detector) described in Hirst *et al.* (2000). This counts and sizes spherical particles above  $2\mu\text{m}$  diameter and counts non-spherical particles. Photodetectors arranged azimuthally at a forward scattering angle give an asphericity value which indicates the dominant water phase in the cloud. A comparison with different probes, carried out in Field *et al.* (2001), estimates the error on the concentration to be at most a possible overestimate by a factor of 3.

- A Nevzorov bulk water probe. Liquid water is measured by a hot wire probe where drops evaporating from the wire surface cause changes in electrical resistance. In totally glaciated conditions, the probe responds to small ice crystals which give a false liquid water content typically 20% of the total water (Korolev *et al.* 1998). The error in mass is around 15%. Total condensed water (TCW) is measured by a hot wire cup which collects drops and ice crystals with an error in mass of 20%.
- A counter-flow virtual impactor (CVI) probe, see Noone *et al.* (1988). Counter-flow of dry air enables only particles with mass greater than that of a  $3.5\mu\text{m}$  radius droplet to enter the probe. Inside the probe the particles are evaporated and residual aerosols measured. In fully glaciated cloud, the residual aerosol concentration should therefore correspond to the ice crystal concentration, assuming one residual per crystal (Ström *et al.* 1997).
- A cloudscope, which is essentially a video camera which views cloud particles impacting on a  $0.2\text{mm}^2$  window. The cloudscope can provide a visual indication of the phase of particles larger than  $10\mu\text{m}$  radius.
- A continuous flow diffusion chamber IN counter similar to the type described by Rogers (1988). This detects deposition and immersion freezing nuclei. Ambient aerosols are subjected to ice supersaturation for several seconds. The humidity is then reduced to below water saturation to remove any liquid drops, and any remaining ice crystals give the IN concentration.

### 3. WAVE CLOUD OBSERVATIONS

This cloud was measured during flight A722 of the INTACC campaign in October 1999, by the Met Office C-130 aircraft (see Field *et al.* (2001) for details on measurements made throughout INTACC). The isolated wave cloud was sampled by aircraft runs at different heights. Each run was straight, level and parallel to the wind. The vertical wind observed during each run (shown in Fig. 1) was typically  $3\text{--}4\text{ ms}^{-1}$ . The cloud was stationary during the two hours that these measurements were taken.

Fig. 2 shows observations from various aircraft probes during some of these runs. No cloud particles are observed until water saturation is reached, when there is a rapid increase in cloud droplet concentration. During the water saturated region, the SID particle concentration remains constant at  $\sim 200\text{ cm}^{-3}$ . The Nevzorov and Johnson-Williams water contents also increase at water saturation, reaching a maximum near the updraught-downdraught boundary. During the downdraught, near the end of the water saturation region the dominant phase of the cloud changes from liquid to ice. At this transition, several changes are observed:

- The environment becomes water subsaturated, but is still ice supersaturated.
- The SID cloud particle concentration falls rapidly to  $\sim 10\text{ cm}^{-3}$ .
- The Nevzorov total and liquid water contents both fall and diverge.
- The average SID asphericity shows a step increase from low values typical of spherical haze particles, to high values typical of aspherical pristine ice crystals.
- On the runs where the aircraft entered the cloud from the downwind end, the cloudscope observations changed from some ice crystals to many small droplets.

Some large particles are, however, observed by the 2D-C probe before this phase transition, so a few ice crystals must have been initiated during the liquid water region. During the ice phase region, the SID concentration agrees with the CVI residual aerosol concentration to within the estimated accuracy of the SID. Disagreement during the liquid

phase is because many of the supercooled haze particles are below the CVI lower size threshold. Runs just above the cloud top encountered high ice supersaturation (the environment was just below water saturation), but no cloud particles were observed. The IN counter was operated just below water saturation, and indicated that the deposition nuclei concentration upwind of the cloud was less than  $0.01 \text{ cm}^{-3}$ .

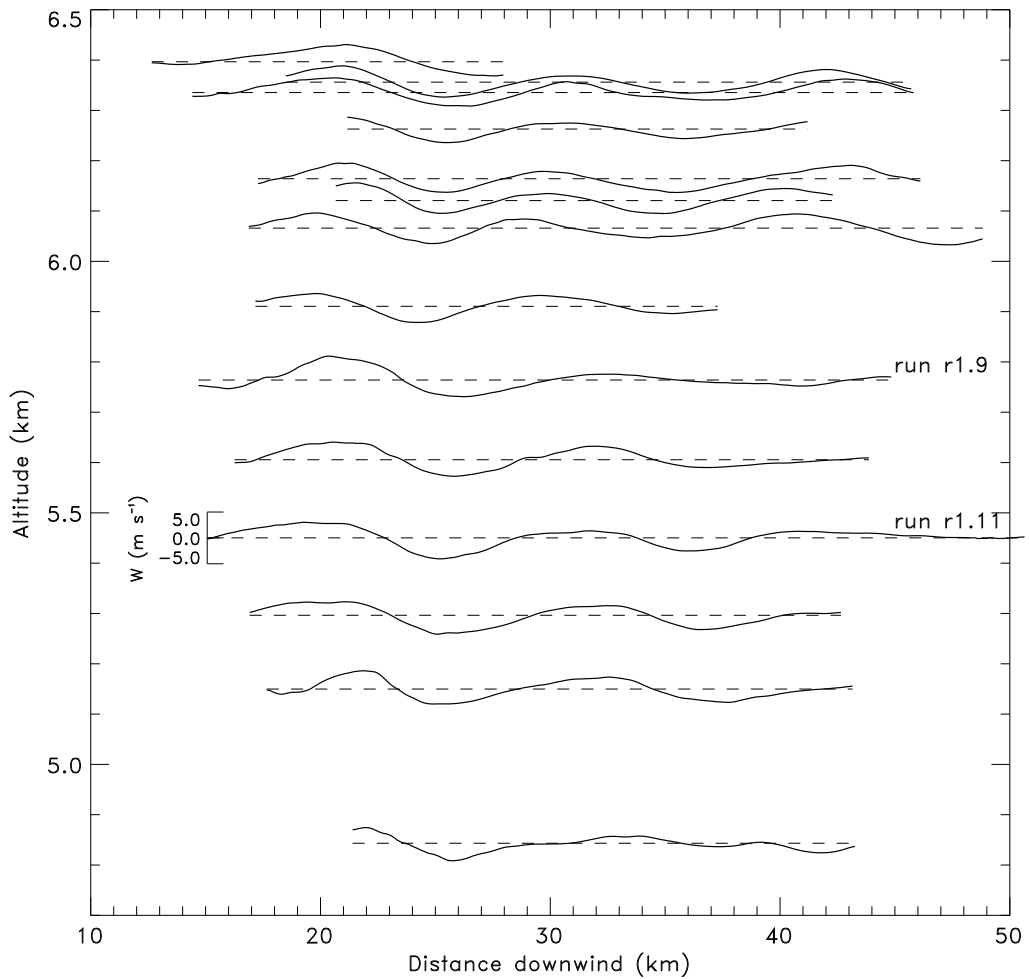


Figure 1. Observed vertical winds for each aircraft run. The top four runs were above the cloud top. Each plot has the same vertical scale as that for run r1.11. The horizontal axis is the distance downwind from an upwind reference point (longitude  $18.5^\circ$ , latitude  $68.25^\circ$ ).

#### 4. WAVE CLOUD SIMULATION

A model has been developed which simulates the microphysical and dynamical aspects of wave clouds. The cloud simulation consists of repeatedly running a parcel model with each parcel starting at a different height and following a different trajectory. Upwind temperature and humidity profiles define the parcel model initial temperature and water vapour mixing ratio, and measured horizontal and vertical winds define the trajectories. All parcel model runs use the same dry CCN size distribution derived from the measured

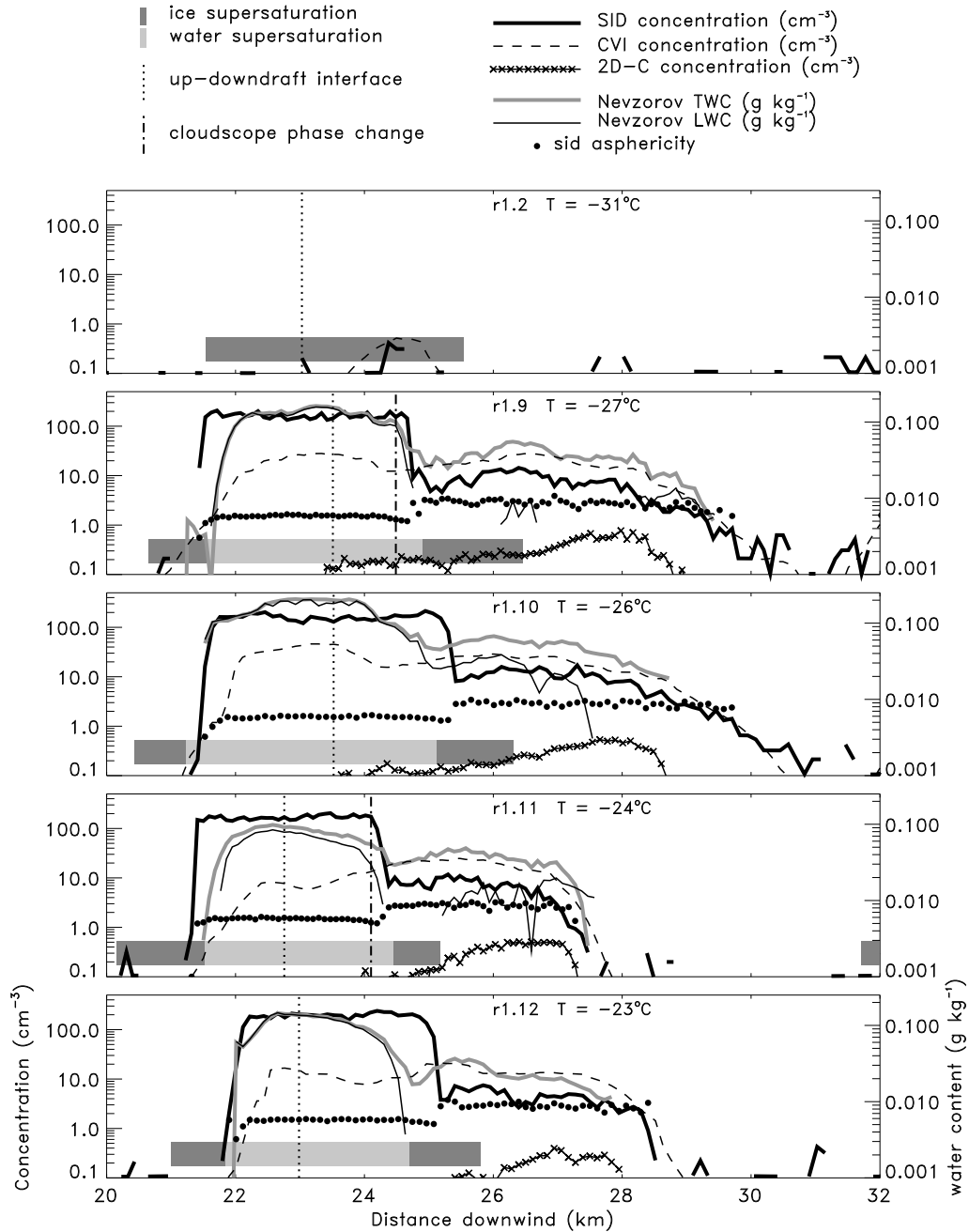


Figure 2. Five of the 14 runs through the wave cloud. The wind is blowing from left to right at 15–20  $\text{ms}^{-1}$ . The top run was just above the cloud top. The horizontal bar shows when the air is above ice saturation (dark grey), or above water saturation (light grey). The vertical dotted line is the updraught-downdraught boundary. The vertical dot-dash line is when the cloudscope shows the dominant phase changing from ice to water. The temperature shown is the mean value over the flight leg. The distance downwind is calculated from an arbitrary reference point upwind of the mountain.

aerosol distribution. Fig. 3 shows some of the parcel trajectories that are used to simulate the wave cloud. Parcels are initialised at an arbitrary location upwind of the mountain corresponding to 15km from the upwind reference point. Data from a set of trajectory simulations are re-sampled onto horizontal levels so as to simulate observations made on aircraft horizontal flight legs.

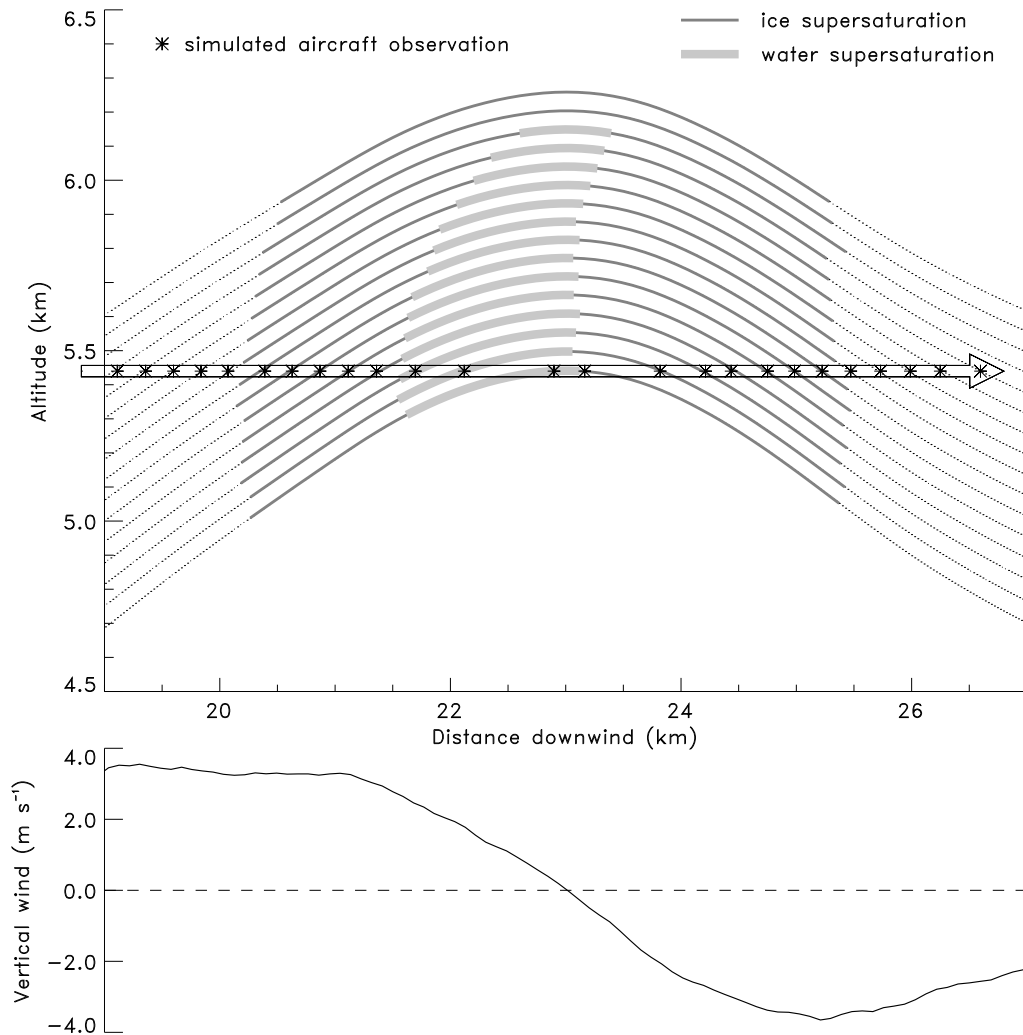


Figure 3. A wave cloud simulation of the aircraft run at the altitude shown by the horizontal arrow. Parcel trajectories are shown by the dotted lines.

(a) *Parcel model description*

The parcel model is an extension of that described in Spice *et al.* (1999), and was used in the GEWEX cloud systems study WG2 cirrus parcel model comparison project described in Lin R-F *et al.* (2000), in which the homogeneous freezing studies all agree closely.

The model considers an adiabatic parcel of air containing a conserved mass of water. A vertical wind time series describes the ascent and descent of the parcel during the model

run. At the start of the model run the dry CCN are deliquesced to the equilibrium haze droplet radii calculated using a Newton-Raphson iteration on the Kohler equation. It is assumed that the CCN have been pre-deliquesced by exposure to high ambient relative humidity. The CCN are either  $\text{H}_2\text{SO}_4$  or  $(\text{NH}_4)_2\text{SO}_4$ , with a Van't Hoff factor of 3.

During the model run, haze and activated cloud droplets share the same bins. The bin radii are explicitly varied in time using the droplet diffusional growth rate equation (Pruppacher and Klett, 1997),

$$r \frac{dr}{dt} = \frac{1}{[F_k + F_d]} \left( \sigma_w - \frac{A_c}{r} + \frac{A_s r_{ccn}^3}{r^3 - r_{ccn}^3} \right) \quad (1)$$

where  $\sigma_w$  is the water supersaturation,  $r$  the droplet radius and  $r_{ccn}$  the radius of the dry CCN. The terms involving  $A_c$  and  $A_s$  relate to curvature and solution effects on the drop's equilibrium vapour pressure.  $F_d$  and  $F_k$  are thermodynamic terms associated with heat conduction and vapour diffusion.  $F_d$  and  $F_k$  contain kinetic correction functions as defined by Fukuta and Walter (1970) to characterise the molecular transfer of heat and vapour. The droplet condensation coefficient  $\alpha_c$  (0.05), the ice deposition coefficient  $\alpha_d$  (0.24), and the thermal accommodation coefficient  $\alpha_t$  (0.7) values are those used in Sassen and Dodd (1988). These correction functions tend to reduce the diffusional growth and evaporation rates.

There are also a fixed number of ice particle radius bins (for these simulations there are 60 ice bins) which are initially empty. The ice particle bin radii are explicitly varied in time using the ice particle diffusional growth rate equation,

$$r_i \frac{dr_i}{dt} = \frac{\sigma_i(C/r_i)}{[F_k + F_d]} \quad (2)$$

where  $\sigma_i$  is the ice supersaturation,  $r_i$  the ice crystal radius, and  $C$  is a constant 'capacitance' used to represent the ice crystal habit (for spherical ice crystals  $C = 1$ ). Ice particles may develop in these bins as a result of primary nucleation processes, either by the homogeneous freezing of supercooled water droplets or by various heterogeneous freezing processes. Ice crystals initiated by vapour deposition onto an IN are placed into the smallest ( $0.1\mu\text{m}$  radius) bin, while droplets that freeze, because of the different ice and droplet diffusional growth rates, are partitioned between two ice particle bins so as to conserve both mass and number concentrations.

During the model run the ice size bins are periodically re-defined to avoid the accumulation of large ice bins, and the current ice crystal population re-distributed amongst the new bins so as to conserve crystal mass and number concentration. The new bin radii are distributed logarithmically from  $0.1\mu\text{m}$  to the maximum crystal size.

The coupled set of differential equations involving temperature, humidity, droplet and ice bin radii and concentrations, are solved using a predictor-corrector integration scheme with a time step of  $\Delta t = 0.01\text{s}$ . Numerical damping is applied for rapidly growing/evaporating haze particles and for the ice nucleation processes, which otherwise would cause instabilities in the model when using this time step.

#### (b) Ice particle nucleation schemes

The homogeneous freezing rate per unit volume of water,  $J$  ( $\text{cm}^3\text{s}^{-1}$ ), is calculated by a fit to the Jeffery and Austin (1997) formulation,

$$T_e < -65 :$$

$$\log(J) = 25.63$$

$$\begin{aligned} -65 \geq T_e \geq -30: \quad \log(J) &= -243.4 - 14.75T_e - 0.307T_e^2 - 0.00287T_e^3 - 0.0000102T_e^4 \\ T_e > -30: \quad \log(J) &= -7.63 - 2.996(T_e + 30) \end{aligned} \quad (3)$$

where  $T_e$  (°C) is the effective temperature.  $T_e$  takes into account the droplet solution concentration and is defined by

$$T_e = T_d + \lambda \delta T \quad (4)$$

where  $T_d$  (°C) is the droplet temperature (which is generally not the same as the parcel temperature),  $\lambda$  quantifies additional non-ideal ionic interactions between the solute and liquid water during droplet freezing, and  $\delta T$  quantifies the melting temperature depression in less strongly bonded impure ice particles.  $\delta T$  is calculated using fits to standard tabulated values (Paul Demott, personal communications). For  $\text{H}_2\text{SO}_4$ ,

$$\delta T = 3.514G + 0.472G^2 + 0.0332G^3 + 0.0251G^4 \quad \text{and} \quad \lambda = 2.0 \quad (5)$$

and for  $(\text{NH}_4)_2\text{SO}_4$ ,

$$\delta T = 0.0220 + 4.12G - 1.331G^2 + 0.668G^3 + 0.125G^4 + 0.0083G^5 \quad \text{and} \quad \lambda = 1.7 \quad (6)$$

where  $G$  is the droplet molality (moles of solute per kg of water). This solution effect reduces the freezing rates of aqueous solution compared to pure water, and can prevent small highly concentrated haze droplets from freezing homogeneously until they become dilute. The droplet freezing rate (number of droplets frozen per unit volume of air per second) for each droplet bin is then,

$$\left. \frac{dN_d}{dt} \right|_{hom} = JV_d N_d \quad (7)$$

where  $N_d$  ( $\text{cm}^{-3}$ ) is the concentration of droplets of volume  $V_d$  ( $\text{cm}^3$ ).

Various heterogeneous ice nucleation schemes are available in the model.

The number concentration of IN that act as either deposition or condensation-freezing nuclei,  $N_{d/cf}$  ( $\text{cm}^{-3}$ ), is described by Meyers *et al.* (1992) and

$$N_{d/cf} = F 10^{-3} \exp(-0.639 + 12.96\sigma_i) \quad (8)$$

where  $\sigma_i$  is the ice supersaturation, and  $F$  is a factor which is adjusted to arbitrarily scale  $N_{d/cf}$ . The ice crystal initiation rate is then,

$$\left. \frac{dN_i}{dt} \right|_{dep} = 12.96 N_{d/cf} \frac{d\sigma_i}{dt} \quad (9)$$

Ice crystals are generated once the ambient humidity is above ice saturation and for a wave cloud, this is always reached before water saturation.

Contact nucleation is incorporated using the aerosol collection rates as described in Young (1974) which include Brownian motion, thermophoretic and diffusiphoretic effects. The number concentration of available contact IN,  $N_{con}$  ( $\text{cm}^{-3}$ ), is set to an arbitrary value rather than using the parametrisation in Young (1974). The collection rates determine at what time during the model run these events occur and reduces the  $N_{con}$  upper limit to the potential ice-crystal concentration. The droplet freezing rate can be approximated for discussion purposes by the form,

$$\left. \frac{dN_d}{dt} \right|_{con} \sim N_d N_{con} \left( A_{br} \frac{r}{r_a^2} - (A_{th} - A_{di}) r \frac{dr}{dt} \right) \quad (10)$$

where  $r$  is the droplet radius,  $r_a$  the aerosol radius.  $A_{br}$ ,  $A_{th}$ ,  $A_{di}$  are positive constants related to Brownian motion, thermophoretic and diffusiophoretic forcing respectively (always  $A_{di} < A_{th}$ ) and depend on the ambient conditions and aerosol composition. This shows that:

- A larger droplet radius increases the collection rate.
- For small aerosol radius, the Brownian motion is dominant.
- For large aerosols when the droplets are evaporating the thermophoretic effect significantly enhances the collection rate.

Immersion freezing is incorporated by using the stochastic hypothesis formulated by Bigg (1953). Freezing results from random formation of a critical size embryo, and the droplet freezing rate is,

$$\left. \frac{dN_d}{dt} \right|_{imm} = V_d N_d B \exp(AT_d - 1) \quad (11)$$

where  $A = 0.66^\circ\text{C}^{-1}$  and  $B = 100 \text{ m}^{-3}\text{s}^{-1}$ . The immersion freezing rate increases for large droplets and for colder temperatures.

(c) *Model initial conditions: CCN spectrum*

The dry CCN size spectrum was derived from upwind aerosol measurements using the PCASP, CN counter, and SID, shown in Fig. 4.

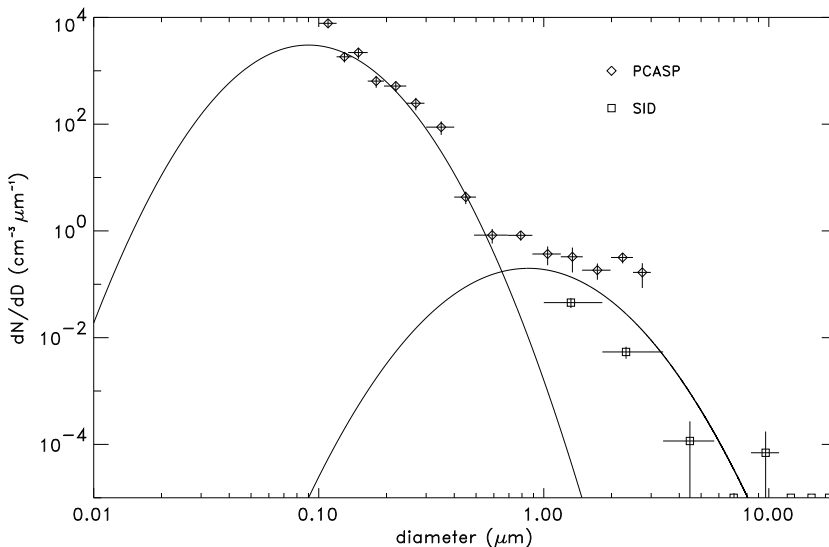


Figure 4. Dry CCN spectrum derived from upwind aerosol measurements, made in clear air using SID and PCASP. The lines are the fitted lognormal functions to the accumulation and coarse mode aerosols.

The CCN were assumed to be hygroscopic spheres of either  $\text{H}_2\text{SO}_4$  or  $(\text{NH}_4)_2\text{SO}_4$ , lognormally distributed with the number of aerosols per unit volume with radius  $r$  to  $r + dr$  given by,

$$N(r)dr = \frac{N_t}{\sqrt{2\pi}} \exp \left[ -\frac{1}{2} \left( \frac{\ln r - \ln r_g}{\ln \sigma} \right)^2 \right] d(\ln r) \quad (12)$$

The PCASP accumulation mode lognormal fit had the constraint that the total number  $N_t$  was that measured by the CN counter (giving  $r_g = 0.11\mu\text{m}$ ,  $\sigma = 1.565\mu\text{m}$ ). The distribution was then binned with 50 logarithmically increasing bin widths to provide the model input. The lognormal distribution of the clear-air SID and PCASP coarse mode aerosols were binned to give a further 10 points for the initial CCN spectrum (where  $N_t = 0.244, r_g = 1.1\mu\text{m}$ ,  $\sigma = 1.657\mu\text{m}$ ).

(d) *Model initial conditions:*

An environmental lapse rate and humidity profile defined at the cloud simulation start distance is used to initialise each parcel model run which starts at a different height. These vertical profiles of temperature and humidity were derived from the measurements made along the horizontal aircraft run. Out of cloud (both upwind and downwind) measurements of temperature and TWC at one second intervals were translated back along streamlines to the upwind start distance. TWC was conserved and latent heat release was taken into account.

Using the observed vertical and horizontal winds to derive the streamlines results in the profiles Figs. 5(a) and 5(b) which have a large scatter. The aircraft kept constant altitude during each run, cutting through many parcel streamlines more than once. Observations from the same streamline should therefore give similar temperature and humidity at the start height.

The scatter in the temperature and humidity profile can be significantly reduced if an empirical offset is added to the vertical wind observations. The profiles Figs. 5(c) and 5(d) were obtained by adding a constant  $0.5\text{ ms}^{-1}$  to the vertical wind. This offset depends on the aircraft run that is being modelled and was typically  $0\text{--}0.5\text{ ms}^{-1}$ . Usually, for wind measurements where the aircraft runs are long, the average vertical wind is subtracted but here the runs are short compared to the horizontal scale of the waves. The mean vertical wind along the flight leg cannot, therefore, be assumed to be zero.

Each parcel model run is initialised with the environmental temperature from a linear fit to the temperature profile and with the humidity from a polynomial fit to the water vapour mixing ratio profile. Fig. 6 shows good agreement between the aircraft observations and model values of vertical wind, temperature and relative humidity along run r1.11. This agreement is expected since the observations were used to initialise the model, but it does show the level of error and self-consistency. The vertical shear of the horizontal wind was taken into account because parcels have large vertical excursions. This wind offset is small compared to the fluctuations in vertical wind, but if the cloud simulation used a non-corrected vertical wind to determine the parcel trajectories, then it would be impossible to match the temperature and humidity along the run using upstream temperature and humidity profiles. The detailed microphysics could not then be accurately simulated.

## 5. MODEL-OBSERVATION COMPARISONS

The key aspects that the model should be expected to reproduce, are:

- Few cloud particles (above  $1\mu\text{m}$  radius) until water saturation is reached.
- Significant liquid water mass (reaching  $0.06\text{--}0.15\text{g kg}^{-1}$ ).
- The dominant phase changing from liquid to ice during the downdraught.
- Ice concentrations of  $\sim 10\text{ cm}^{-3}$ , for droplet concentrations of  $\sim 200\text{ cm}^{-3}$ .

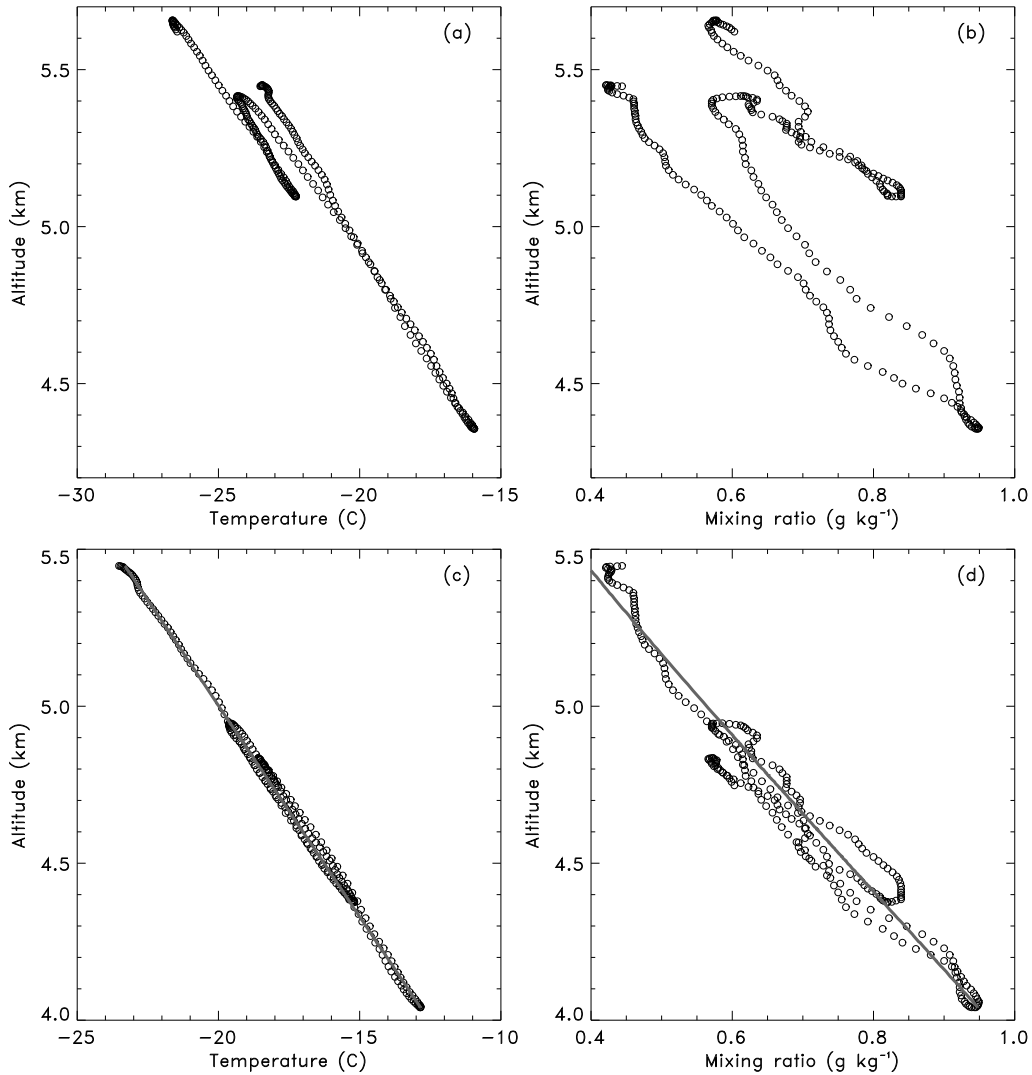


Figure 5. Temperature and humidity profiles defined at the cloud simulation start distance, derived from aircraft observations made along run r1.11. For (a) and (b) no vertical wind offset was applied (a) and (b), while for (c) and (d) the offset was  $0.5 \text{ ms}^{-1}$ . The lines are the fitted environmental lapse rate (linear fit) and the water vapour mixing ratio (polynomial fit) that are used for model initialisation.

Simulations of a series of aircraft runs through the wave cloud were made using various primary ice nucleation schemes with the aim of determining the ice nucleation characteristics which best match the observed data. Fig. 7 and Fig. 8 show, for aircraft run r1.11, a series of simulations each using a different ice nucleation scheme. The coldest temperature reached by the parcel for this aircraft run is around  $-30^\circ\text{C}$ , so homogeneous freezing is negligible (the droplet-environment temperature difference due to evaporation is small). The simulation with only homogeneous freezing (Figs. 7(a) and 7(b)) shows that for the liquid water part of the cloud, the start and end distance and total water content are well modelled. Even for the highest run through the cloud, the model predicts little homogeneous freezing.

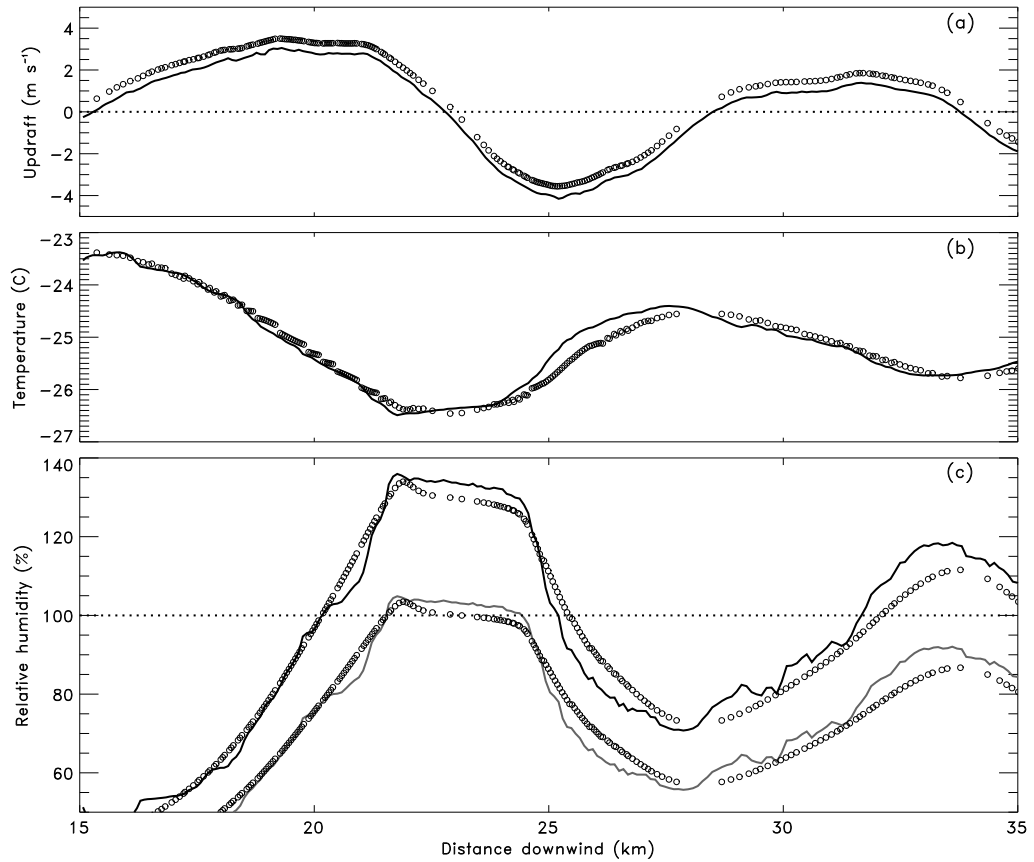


Figure 6. Thermodynamic *in-situ* observations made along run r1.11 and the model simulation of, (a) the vertical wind, (b) temperature, and (c) relative humidities w.r.t. water and ice. The solid lines are the aircraft observations. Each symbol is from a model streamline intersecting the aircraft altitude. A constant offset of  $0.5 \text{ ms}^{-1}$  has been added to the vertical wind.

Deposition nucleation (Figs. 7(c) to 7(f)) is not expected to be the dominant mode. This is because the IN counter measured few deposition nuclei, runs immediately above cloud top encountered ice saturation but no ice was observed, and deposition nuclei will tend to be activated before the liquid water phase (in a wave cloud, ice saturated is always reached before water saturation). Increasing the deposition/condensation-freezing rate by using  $F = 5$  (Figs. 7(c) and 7(d)) gives the required ice water content but there are too few ice crystals, while increasing it by using  $F = 100$  (Figs. 7(e) and 7(f)) generates too much ice water mass from the required ice number concentration. The 2D-C probe does detect  $\sim 0.1 \text{ cm}^{-3}$  large ice crystals during the liquid water part of the cloud, so a few of the observed ice crystals could be initiated by deposition nucleation.

Contact nucleation (Figs. 8(a) and 8(b)) where Brownian motion dominates the collection rates (small aerosol radius) can achieve the measured ice concentration if there is a large contact aerosol concentration. While some ice crystals are formed by collisions with haze particles, most are formed when the droplets are larger. However the ice water mass is still too high and the liquid water growth is inhibited.

Immersion freezing (Figs. 8(c) and 8(d)) forms ice crystals after the peak of the liquid water cloud when the droplets are large and the temperature is coldest. To get

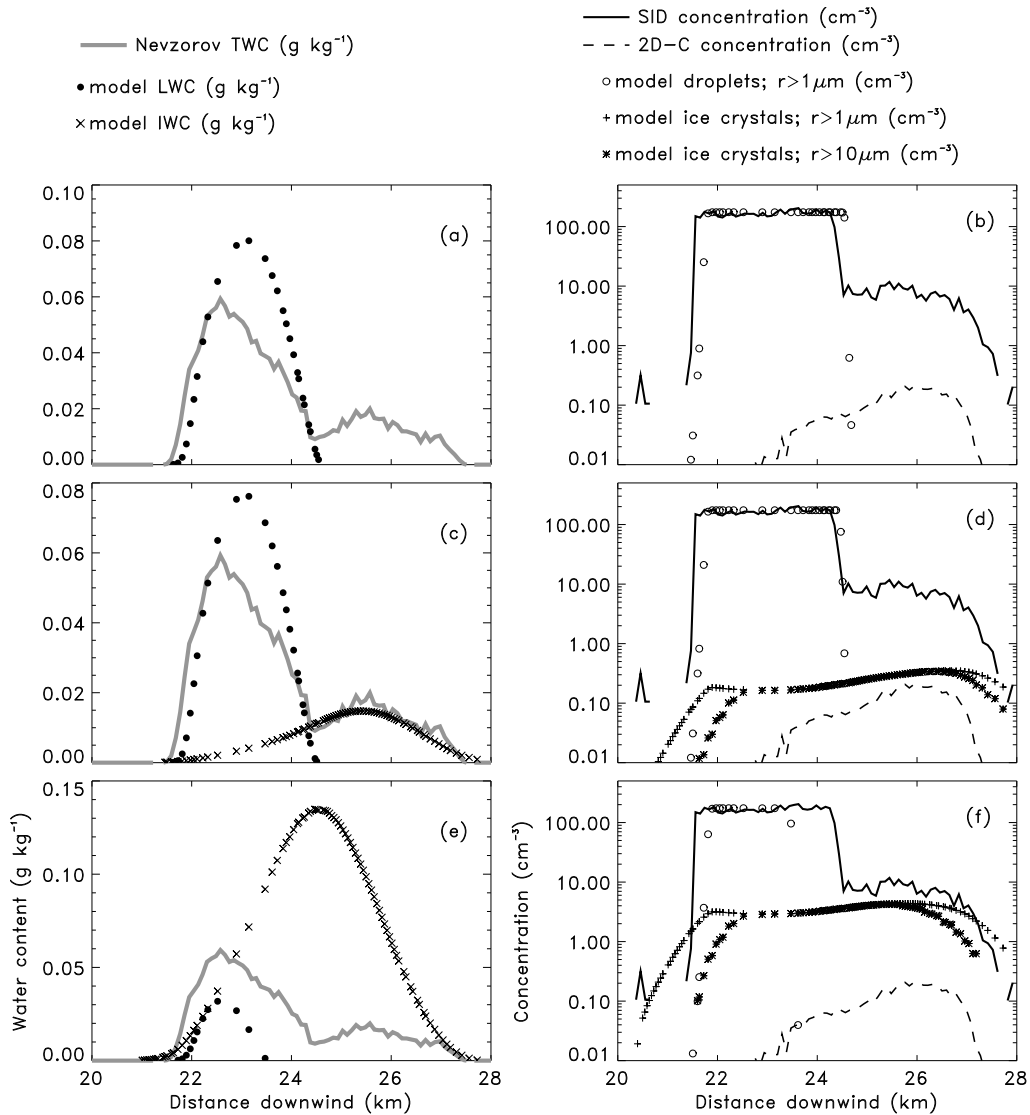


Figure 7. A comparison of aircraft observations from run r1.11 with numerical model data extracted for the same altitude, showing ice/liquid water contents (a,c,e) and droplet/ice number concentrations (b,d,f). The ice nucleation schemes are; (a,b) homogeneous freezing of  $(\text{NH}_4)\text{SO}_4$  solution droplets, (c,d) combined deposition and condensation-freezing where  $F = 5$ , and (e,f) where  $F = 100$ .

the measured ice crystal concentration the constant  $B$  is increased to  $10^4 \text{ m}^{-3}\text{s}^{-1}$  since there are large uncertainties on  $B$  which depends on the droplet solution. The ice water mass is still too high however, but the liquid water peak is well matched.

Contact nucleation (Figs. 8(e) and 8(f)), where the thermophoretic effect enhances the collection rates (large aerosol radius) causes ice to be formed during the rapid droplet evaporation region in the downdraught. However the collision rate is too low, so that even with a very high aerosol concentration, the modelled ice concentration is an order of magnitude too small.

An arbitrary 'evaporation-onset' nucleation scheme (Figs. 8(g) and 8(h)) can be used

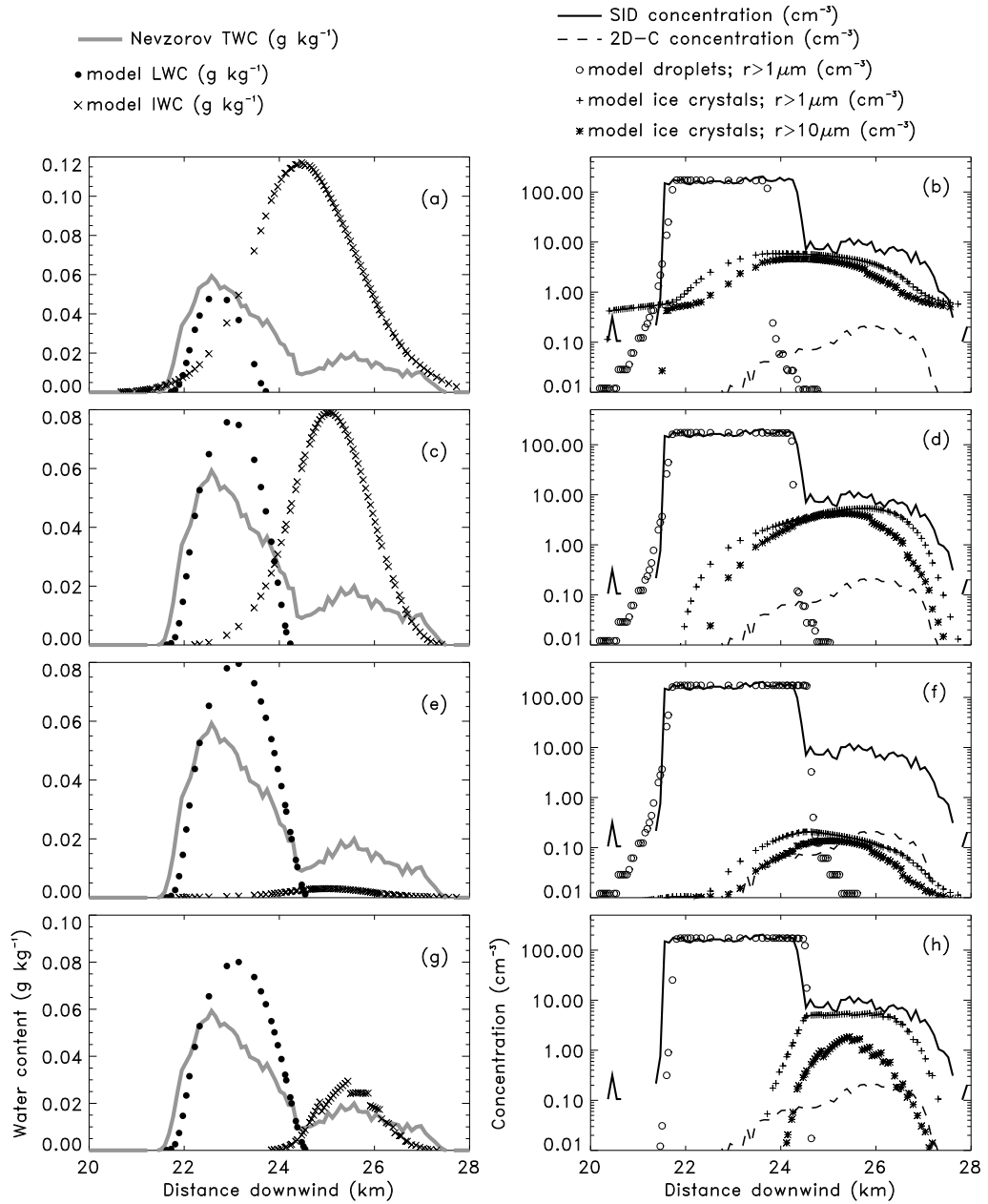


Figure 8. As in fig. 6, but with ice nucleation schemes; (a,b) contact nucleation where  $r_a = 0.01 \mu\text{m}$ ,  $N_c = 400 \text{cm}^2$ , (c,d) immersion-freezing where  $B = 10^4 \text{m}^{-3} \text{s}^{-1}$ , (e,f) thermophoretically enhanced contact nucleation where  $r_a = 0.1 \mu\text{m}$ ,  $N_c = 400 \text{cm}^2$ , and (g,h) evaporation-onset freezing where  $J_e 2 \times 10^{14} \text{m}^{-3} \text{s}^{-1}$ .

to show that to achieve the observed liquid and ice water mass and concentration characteristics, most ice crystals must be formed near the end of the liquid water evaporation region. Because of the very rapid increase in droplet solution concentration once water subsaturation is reached, a concentration threshold was used to activate the freezing of each droplet bin. Similar to homogeneous freezing, a stochastic freezing rate is defined by,

$$\frac{dN_d}{dt} \Big|_{evap} = V_d N_d J_e \quad (13)$$

where  $J_e$  is a constant ( $2 \times 10^{14} \text{ m}^{-3} \text{ s}^{-1}$ ) arbitrarily chosen to give the observed ice crystal concentration. For simplicity  $J_e$  is not defined as a function of temperature. This nucleation scheme is not describing any particular physical mechanism, and the choice of the freezing rate equation is not critical—its just a method of generating the observed ice crystal concentration at a specific time and within a short duration. The much more rapid rate of increase in ice crystal concentration for this simulation is clearly shown in Fig. 8(h). The LWC and IWC for parcels following the streamlines are shown in Fig. 9.

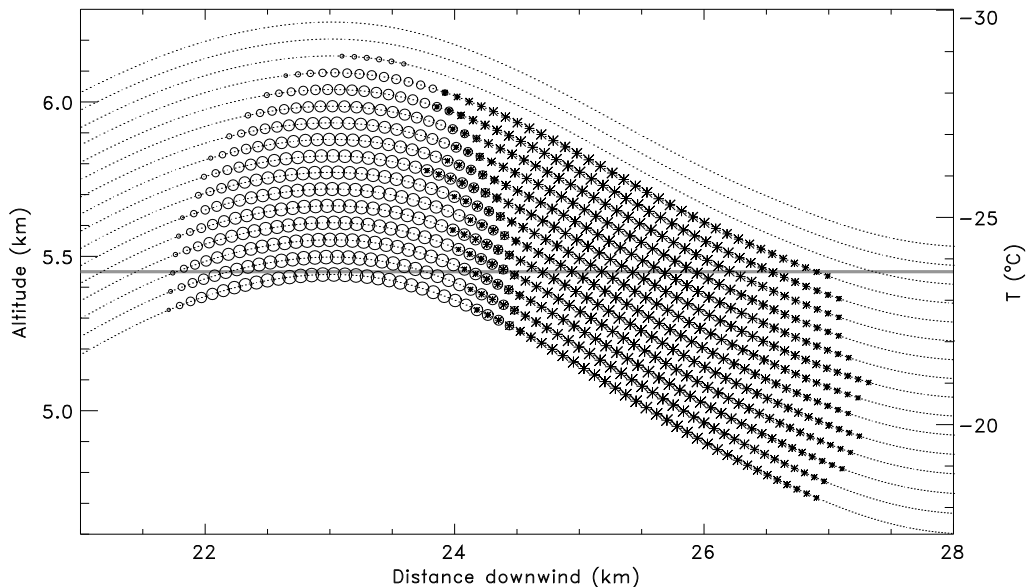


Figure 9. A wave cloud simulation of the aircraft run r1.11, at the altitude marked by the grey line. Only the evaporation-onset nucleation scheme is active. Parcel trajectories are shown by the dotted lines (only every 5th trajectory is shown). Circles are drawn when there is significant liquid water, stars when there is significant ice. The size of the symbol represent the amount of water mass. There is an upwind liquid water region, a narrow mixed phase region, and an ice tail in the downdraft region. The right ordinate is the mean temperature in the undisturbed environment, not the parcel temperature in the cloud.

The tendency for ice nucleation schemes that create ice crystals later in the wave cloud to better match the observations is shown more clearly in Fig. 10. The ice concentration and water contents plotted are the maximum obtained in the downwind region of the cloud. Results from cloud simulations using the same ice nucleation scheme but with different 'scaling constants' ( $F$ ,  $N_c$ ,  $B$ ,  $J_e$ ) lie along the same line. Where the IN activation occurs later in the cloud, this line moves further to the right. The position along the line is determined by:

- For deposition nucleation, the factor  $F$  which increases the number  $N_{d/cf}$  of IN that

are activated.

- For contact nucleation, the total number  $N_c$  of aerosol available.
- For immersion freezing, the droplet freezing activity  $B$ .
- For evaporation-onset freezing, the constant  $J_e$ .

These all have large uncertainties so the actual position along the line is not well constrained, although the depletion of liquid water puts a constraint on the upper limit.

Changing some of the constants used in the parcel model tends to move these lines further from the ice mass/concentration observation. The 'capacitance'  $C$  used in the ice crystal growth rate equation is nominally set to  $C = 0.3$  to represent non-spherical ice crystals. Assuming a spherical ice crystal habit by setting  $C = 1.0$ , increases the ice growth and moves the deposition line further to the left, giving higher IWC for a given number concentration (shown by the large vertical arrow in Fig. 10). The ice crystal density is nominally set to  $1.0 \times 10^3 \text{ kg m}^{-3}$ . Reducing the density to  $0.5 \times 10^3 \text{ kg m}^{-3}$  also increases the ice growth and moves the deposition line further to the left (shown by the small vertical arrow in Fig. 10). Changing the coefficients  $\alpha_c$ ,  $\alpha_d$  and  $\alpha_t$  used in the calculation of the kinetic correction functions  $F_d$  and  $F_k$  within reasonable limits has only a small effect. The similar gradients might imply that these lines are a characteristic of the wave cloud environmental conditions.

## 6. DISCUSSION AND CONCLUSION

The environmental conditions in wave clouds are forced by the dynamics. To accurately simulate wave cloud observations, it is therefore critical to know the wind field over the height of the cloud, in addition to good upstream temperature and humidity profiles. Aircraft vertical wind measurements commonly show systematic biases of up to  $0.5 \text{ ms}^{-1}$ . It is important that this be removed prior to the use of wind data to calculate air parcel trajectories, otherwise the humidity will be simulated incorrectly when the height displacement of the parcel is estimated by integrating the vertical velocity.

Observations indicate, and modelling confirms, that for the wave cloud measured during flight A722, the presence of water droplets is a prerequisite for ice crystal generation. This agrees with the mountain cap cloud observations of Cooper and Vali (1981).

The droplet temperatures were too warm ( $T_d > -30 \text{ }^\circ\text{C}$ ), even during rapid evaporation, for significant homogeneous freezing. The significant liquid water mass implies that the dominant heterogeneous nucleation mode occurring in this cloud is not deposition nucleation. Deposition IN will activate before water supersaturation is reached and a large number of rapidly growing ice crystals will inhibit droplet growth. Both condensation-freezing and stochastic immersion freezing are also not the dominant nucleation mode. Changing the ice crystal capacitance and density from the model nominal values makes this conclusion more robust. Thermophoretically enhanced contact nucleation occurs during rapid droplet evaporation but the collision rates are too low.

The wave cloud model cannot reproduce, using any of the usual heterogeneous nucleation modes, both the observed peak ice number concentration and ice water content while not reducing the peak LWC in the liquid water part of the cloud. To simulate both of these simultaneously, most of the ice nucleation must occur rapidly at a critical time during the evaporation of the liquid droplets. The onset of ice growth must be delayed so that the time available for growth is restricted which enables the IWC to be kept within bounds. This is much more rapid and localised than any of the standard heterogeneous ice nucleation mechanisms. This conclusion depends on the observations of high ice concentrations of typically  $10 \text{ cm}^{-3}$  being correct. The SID droplet concentration is well

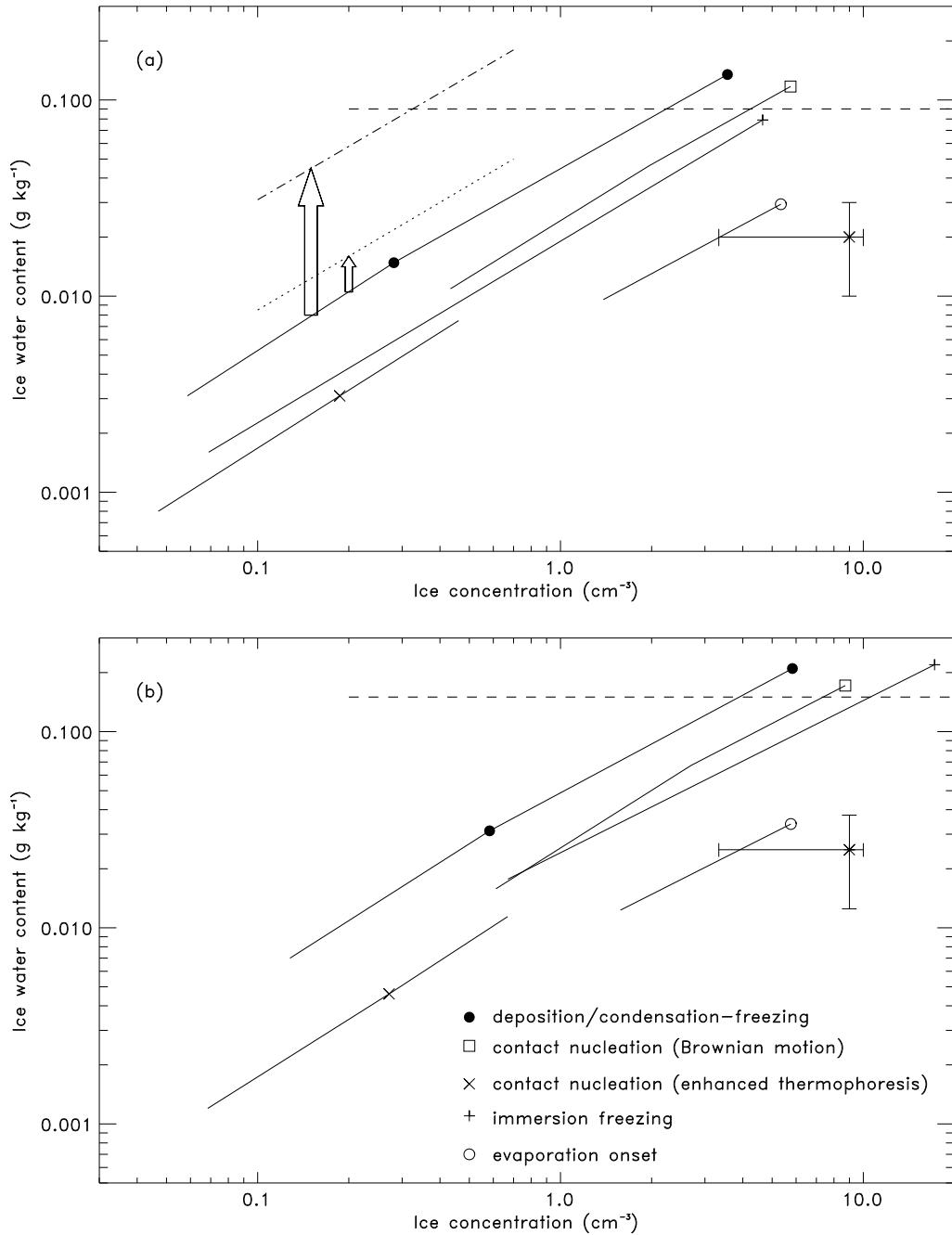


Figure 10. Simulated peak ice values for aircraft run r1.11 (a) and for run r1.9 (b). Results from each heterogeneous nucleation mode lie along a different line. The symbols are for those runs that are shown in Fig. 7 and Fig. 8. Deposition/condensation-freezing lie along the line with ● symbols, contact nucleation where Brownian motion dominates ( $r_a = 0.01\mu\text{m}$ ) with □ symbols, thermophoretically enhanced contact nucleation ( $r_a = 0.1\mu\text{m}$ ) with × symbols, immersion freezing with + symbols, and evaporation-onset freezing with ○ symbols.

Reducing the ice crystal density to  $0.5\text{ kg m}^{-3}$  moves the deposition/condensation-freezing onto the dotted line. Increasing the ice crystal capacitance to  $C = 1.0$  moves the deposition/condensation-freezing onto the dot-dash line. The observed peak ice mass-concentration are the \* symbols with estimated 95% confidence limit error bars. IWC in excess of the dashed line results in significant depletion of LWC in the liquid water part of the cloud.

modelled, and the SID and CVI agree well in the ice phase. Additionally, during another INTACC flight where the temperature was low enough for homogeneous freezing to be dominant, the ice concentration was similar to the initial droplet concentration (see Field *et al.* 2001).

Most of the ice nucleation must occur at a critical time during evaporation of the liquid droplets in the downdraught. The environmental conditions in the wave cloud during this critical time can be similar to those near the top of altostratus cloud layers where there is mixing with dry air (with comparable vertical winds and evaporation regions). It is, therefore, reasonable to assume that the ice nucleation mechanism that occurs in this wave cloud may also be occurring more generally in clouds within the same temperature range.

## 7. ACKNOWLEDGEMENTS

Financial support for this work was given by the EU under the contract ENV4-CT97-0549. Support is acknowledged from the Swedish Air Force Jamtland Air Wing (F4) in Ostersund, Sweden, and from the Swedish Meteorological service. The Royal Air Force aircrew and ground crew of the Met Office C-130 aircraft are also thanked. Finally the valuable guidance of Phil Brown is acknowledged.

## REFERENCES

- |  |      |  |
|--|------|--|
| Beard, K. V.   | 1992 | Ice initiation in warm-base convective clouds: an assessment of microphysical mechanisms. <i>Atmos. Res.</i> , <b>28</b> , 125–152         |
| Bigg, E. K.  | 1953 | The formation of atmospheric ice crystals by the freezing of droplets. <i>Q. J. R. Meteorol. Soc.</i> , <b>79</b> , 510–519                |
| Cooper, W. A. and Vali, G.   | 1981 | The origin of ice in mountain cap clouds. <i>J. Atmos. Sci.</i> , <b>38</b> (6), 1244–1259   |
| DeMott, P. J.  | 1990 | An exploratory study of ice nucleation by soot aerosols. <i>J. Appl. Meteorol.</i> , <b>29</b> , 1072–1079                                 |
| Field, P. R., Cotton, R. C.,<br>Noone, K., Glantz, P.,<br>Keye, P. H., Hirst, E.,<br>Greenaway, R. S., Jost, C.,<br>Gabriel, R., Reiner, T.,<br>Andreae, M.,<br>Saunders, C. P. R.,<br>Archer, A., Choullarton, T.,<br>Smith, M., Brooks, B.,<br>Hoell, C. Bandy, B.,<br>Johnson, D. and<br>Heymsfield, A. | 2001 | Ice nucleation in orographic wave clouds: Measurements made during INTACC. <i>Q. J. R. Meteorol. Soc.</i> , <b>127</b> , 1493–1512         |
| Fukuta, N. and Walter, L. A.   | 1970 | Kinetics of hydrometeor growth from a vapor-spherical model. <i>J. Atmos. Sci.</i> , <b>27</b> , 1160–1172                                 |
| Heymsfield, A. J.,<br>Miloshevich, L. M.   | 1993 | Homogeneous ice nucleation and supercooled liquid water in orographic wave clouds. <i>J. Atmos. Sci.</i> , <b>50</b> (15), 2335–2353       |
| Hirst, E., Keye, P. H.,<br>Greenaway, R. S.,<br>Field, P. R. and Johnson,<br>D. W.   | 2001 | Discrimination of micrometre-sized ice and supercooled droplets in mixed phase clouds. <i>Atmos. Environ.</i> , <b>35</b> , 33–47          |
| Jeffery, C. A. and Austin, P. H.   | 1997 | Homogeneous nucleation of supercooled water: Results from a new equation of state. <i>J. Geophys. Res.</i> , <b>102</b> (D21), 25269–25279 |

- Jensen, E. J., Toon, O. B., Tabazadeh, A., Sachse, G. W., Andersen, B. E., Chan, K. R., Twohy, C. W., Gandrud, B., Aulenbach, S. M., Heymsfield, A., Hallet, J. and Gary, B. 1998 Ice nucleation processes in upper tropospheric wave clouds observed during SUCCESS. *Geophys. Res. Lett.*, **25**(9), 1363–1366
- Khain, A., Ovtchinnikov, M., Pinsky, M., Pokrovsky, A. and Krugliak, H. 2000 Notes on the state-of-the-art numerical modeling of cloud microphysics. *Atmos. Res.*, **55**, 159–224
- Korolev, A. V., Strapp, J. W., Isaac, G. W. and Nevzorov, A. N. 1998 The Nevzorov airborne hot-wire LWC-TWC probe: Principle of operation and performance statistics. *J. Atmos. Oceanic Technol.*, **15**, 1495–1510
- Meyers, M. P., DeMott, P. J. and Cotton, W. R. 1992 New primary ice-nucleation parameterizations in an explicit cloud model. *J. Appl. Meteorol.*, **31**, 708–721
- Noone, K. J., Ogren, J. A., Heintzenberg, J., Charlson, R. J. and Covert, D. S. 1988 Design and calibration of a counterflow virtual impactor for sampling of atmospheric fog and cloud droplets. *Aerosol Sci. and Technol.*, **8**, 235–244
- Lin, R. L., Starr, D., DeMott, P. J., Cotton, R. J., Jensen, E. and Sassen, K. 2000 Cirrus parcel model comparison project phase 1. Pp.1221–1224 in Proceedings of the 13th conference on clouds and precipitation, Reno, Nevada, UAS, August 14–18
- Pruppacher, H. R. 1995 A new look at homogeneous ice nucleation in supercooled water drops. *J. Atmos. Sci.*, **52**, 1924–1933
- Pruppacher, H. R. and Klett, J. D. 1997 *Microphysics of clouds and precipitation. 2nd edn.* Oxford Press, 919 p
- Quante, M., Brown, P. R. A., Baumann, R., Guillemet, B. and Hignett, P. 1996 Three-aircraft intercomparison of dynamical and thermodynamical measurements during the pre-EUCREX campaign. *Beitr. Phys. Atmosph.* **69**(1), 129–146
- Rogers, D. C. 1988 Development of a continuous flow thermal diffusion chamber for ice nucleation studies. *Atmos. Res.* **22**, 149–181
- Rogers, D. C., Demott, P. J., Kreidenweis, S. M. and Chen, Y. 1998 Measurements of ice nucleating aerosols during SUCCESS. *Geophys. Res. Lett.*, **25**(0), 1383–1386
- Rogers, D. P., Johnson, D. W. and Friehe, C. A. 1995 The stable internal boundary layer over a coastal sea. Part 1: Airborne measurements of the mean and turbulence structure. *J. Atmos. Sci.*, **52**(6), 667–683
- Rosinski, J., Morgan, G. 1991 Cloud condensation nuclei as a source of ice-forming nuclei in clouds. *J. Aerosol Sci.*, **22**, 123–133
- Sassen, K., Dodd, G. C. 1988 Homogeneous nucleation rate for highly supercooled cirrus cloud droplets. *J. Atmos. Sci.*, **45**, 1357–1369
- Spice, A., Johnson, D. W., Brown, P. R., Darlison, A. G. and Saunders, C. P. R. 1999 Primary ice nucleation in orographic cirrus clouds: A numerical simulation of the microphysics. *Q. J. R. Meteorol. Soc.*, **125**, 1637–1667
- Tinsley, B. A., Rohrbaugh, R. P., Hei, M. and Beard, K. V. 2000 Effects of image charges on the scavenging of aerosol particles by cloud droplets and on droplet charging and possible ice nucleation schemes. *J. Atmos. Sci.*, **57**, 2118–2134
- Young, K. C. 1974 The role of contact nucleation in ice phase initiation in clouds. *J. Atmos. Sci.*, **31**, 768–776